Multiple Lattice Instabilities and Complex Ground State in Cs$_2$AgBiBr$_6$

Xing He,[1] Matthew Krogstad,[2,3] Mayanak K. Gupta,[1,4] Tyson Lanigan-Atkins,[1] Chengjie Mao,[5]
Feng Ye,[6] Yaohua Liu,[6] Tao Hong,[6] Songxue Chi,[6] Haotong Wei,[7] Jinsong Huang,[7]
Stephan Rosenkranz,[2] Raymond Osborn,[2] and Olivier Delaire[1,5,8,*]

[1]*Mechanical Engineering and Materials Science, Duke University, Durham, North Carolina, USA*

[2]*Materials Science Division, Argonne National Laboratory, Lemont, Illinois, USA*

[3]*X-ray Sciences Division, Argonne National Laboratory, Lemont, Illinois, USA*

[4]*Solid State Physics Division, Bhabha Atomic Research Centre, Mumbai 400085, India*

[5]*Department of Chemistry, Duke University, Durham, North Carolina, USA*

[6]*Neutron Scattering Division, Oak Ridge National Laboratory, Oak Ridge, Tennessee, USA*

[7]*Applied Physical Sciences, University of North Carolina at Chapel Hill, Chapel Hill, North Carolina, USA*

[8]*Department of Physics, Duke University, Durham, North Carolina, USA*

Metal-halide perovskites (MHPs) are attracting considerable interest for optoelectronic applications, with Cs$_2$AgBiBr$_6$ one of the main contenders among lead-free systems. Cs$_2$AgBiBr$_6$ crystallizes in a nominally double-perovskite structure, but exhibits a soft lattice with large atomic fluctuations characteristic of MHPs. While crucial to understand electron-phonon and phonon-phonon couplings, the spatiotemporal correlations of these fluctuations remain largely unknown. Here, we reveal these correlations using comprehensive neutron and x-ray scattering measurements on Cs$_2$AgBiBr$_6$ single crystals, complemented with first-principles simulations augmented with machine-learned neural-network potentials. We report the discovery of an unexpected complex modulated ground-state structure containing several hundred atoms, arising from a soft-phonon instability of the low-temperature tetragonal phase. Further, our experiments and simulations both reveal extensive correlated two-dimensional fluctuations of Br octahedra at finite temperature, arising from soft optic phonons that are strongly broadened by anharmonicity, reflecting very shallow potential wells. These results provide new insights into the atomic structure and fluctuations in MHPs, critical to understand and control their thermal and optoelectronic properties.

I. INTRODUCTION

Metal-halide perovskites (MHPs) exhibit outstanding performance for photovoltaic, optoelectronic, and radiation detection applications [1–5], and also attract interest for thermoelectric [6,7] or thermochromic applications [8]. The efficiency of MHP solar cells has drastically improved over the last decade [9,10], enabled by their excellent carrier-transport properties, including extremely long carrier lifetimes [4,11–15]. All-inorganic MHPs present advantages in terms of stability, and enable the growth of large single crystals with larger band gaps well suited for radiation detection or thermochromic applications

*olivier.delaire@duke.edu

[8,16–18], and their fundamental photophysics could actually be superior to those of hybrid systems [19]. Lead-free MHPs, such as Cs$_2$AgBiBr$_6$, are attracting particular interest because of their lower toxicity and improved stability in air compared to lead-based systems [20–24]. Replacing Pb^{2+} in CsPbBr$_3$ with Ag$^+$ and Bi^{3+} lowers the band gap and improves stability [20,21,25,26]. Further, extremely long photocarrier lifetimes were reported [14,20,21].

Importantly, several studies of inorganic MHPs highlighted lattice instabilities of the halide framework, and the importance of strong phonon anharmonicity to understand the electron-phonon coupling, itself key to rationalize the optoelectronic response [27–30]. Further, studies investigated competing low-energy lattice instabilities, resulting from many shallow local minima in the potential energy surface [31–35], and highlighted the coupling between these instabilities and the electronic states at the edges of the band gap [31,34,36–40]. Recent studies suggest that low-energy phonons and tilt modes couple to electronic band renormalization and excitons in MHPs

[41,42]. In $Cs_2AgBiBr_6$ in particular, a direct link was proposed between the structural and optical properties and the strong electron-phonon coupling [8,24,26,43–47]. Moreover, recent studies suggested that atomic vibrations could broaden the conduction-band edge and reduce the band gap in $Cs_2AgBiBr_6$ [48], while enhancing the band gap in single-halide perovskites [49]. Phonon anharmonicity is also crucial to understand the formation and hopping of polarons [50–52] and ultralow thermal conductivity [53] in $Cs_2AgBiBr_6$. Yet, a detailed understanding of structural dynamics and phonons in $Cs_2AgBiBr_6$ remains elusive owing to a lack of momentum-resolved measurements on single crystals.

Large amplitude atomic fluctuations in MHPs arise from shallow and anharmonic potentials, which also result in very low thermal conductivities and large thermal expansion coefficients [6,28,54–59]. For instance, $Cs_2AgBiBr_6$ is predicted to exhibit ultralow lattice thermal conductivity, which is of fundamental interest and also offers promise for thermoelectric applications [6,30,60,61]. Further compounding the need for detailed structural studies, several MHPs were recently predicted to exhibit complex ground states with large unit cells [34]. Strongly anharmonic phonons and surprising two-dimensional correlations of Br octahedra tilts were recently revealed in $CsPbBr_3$ [30], but it remains to be established whether these unusual dynamics also arise in Pb-free MHPs. Thus, understanding the atomic structure and dynamics of $Cs_2AgBiBr_6$ is critical to rationalize its attractive properties, and to provide insights in the atomic structure and dynamics of the broader MHP family.

Here, we report the first momentum-resolved investigation of the crystal structure and phonons in $Cs_2AgBiBr_6$ single crystals using inelastic neutron scattering (INS) and diffuse scattering of both neutrons and x rays. Our experiments are complemented with first-principles simulations of anharmonic phonons and structural distortions, extended to large simulation scales with a surrogate neural-network potential derived from machine learning. Our experiments and simulations both reveal a surprisingly complex ground state, and pervasive two-dimensional (2D) correlated fluctuations of Br octahedra tilts. We note that during paper preparation, a phase transition at $T \sim 38$ K was reported based on Raman spectroscopy, supporting our findings of symmetry-lowering transition into a distorted ground state [62].

II. RESULTS AND DISCUSSION

The average structure of $Cs_2AgBiBr_6$ is cubic double-perovskite ($Fm\bar{3}m$) at room temperature [22,24,63]. Compared to single-halide perovskites (ABX_3 prototype, e.g., $CsPbBr_3$), the conventional cell of $Cs_2AgBiBr_6$ has doubled lattice constants and contains 40 atoms, while the primitive cell of the face-centered-cubic (FCC) lattice contains ten atoms. The Ag^+ and Bi^{3+} ions form an ordered rock-salt sublattice on the B site of the parent single perovskite. On cooling, $Cs_2AgBiBr_6$ undergoes a second-order phase transition at $T_{c1} \simeq 122$ K to a tetragonal structure with space group $I4/m$, which was proposed to arise from the freezing of a zone-center soft-mode (out-of-phase Br octahedra rotations about the c axis, $a^0a^0c^-$ in Glazer notation) [24,61,63]. As shown in Figs. 1(a) and 1(b), the resulting octahedral rotations about the c axis create adjacent layers perpendicular to this axis having opposite phase. A recent pair distribution function (PDF) study reported local distortions under high pressure but present even at ambient condition, although the associated time scale was not investigated [64].

A. Single-crystal diffuse scattering

Neutron diffuse scattering measurements were conducted on a single crystal (mass approximately 0.2 g) as a function of temperature using CORELLI at the Spallation Neutron Source. CORELLI uses a wide wavelength band to efficiently map large swaths of wave vectors **Q** in reciprocal space, but also enables the discrimination of quasielastic versus inelastic signals with a resolution of approximately 1 meV (for incident neutron energy at 30 meV), through the use of a semirandom chopper and cross-correlation (CC) technique [65]. Large **Q** volumes of diffuse x-ray scattering (integrating over the phonon energy spectrum) were also collected with hard x rays ($E = 87.0$ keV) on Sector 6-ID-D at the Advanced Photon Source (crystal thickness approximately 500 µm). Sharp Bragg peaks at integer (H, K, L) in both neutron and x-ray experiments indicate the high quality of the crystals and the absence of extra grains.

Figure 1 illustrates the cubic and tetragonal average crystal structures (a),(b), the correspondence between single and double perovskite Brillouin zones (BZs) in (c),(d), and shows several diffuse scattering maps extracted from CORELLI data volumes in (e)–(h). At all temperatures, weak superstructure peaks are observed at (H, K, L) all odd (double-perovskite notation), equivalent to R points of the single-perovskite BZ, corresponding to the rock-salt ordering of Ag^+ and Bi^{3+} ions on the perovskite B-site sublattice. Strikingly, in the cubic phase, rods of diffuse scattering intensity are observed in reciprocal planes $L =$ odd in double-perovskite notation, such as $L = 1$ in Figs. 1(e) and 1(f), reminiscent of recent observations in $CsPbBr_3$ [30]. The rod intensity increases upon cooling in the cubic phase, reaching a maximum just above T_{c1}, as seen in Figs. 1(e) and 1(f) (see also Figs. S4 and S5 within the Supplemental Material [66]). The rods remain faintly visible at 100 K in the tetragonal phase, see Fig. 1(g). While they are observed for CORELLI CC either on or off, the diffuse rods are more intense in the
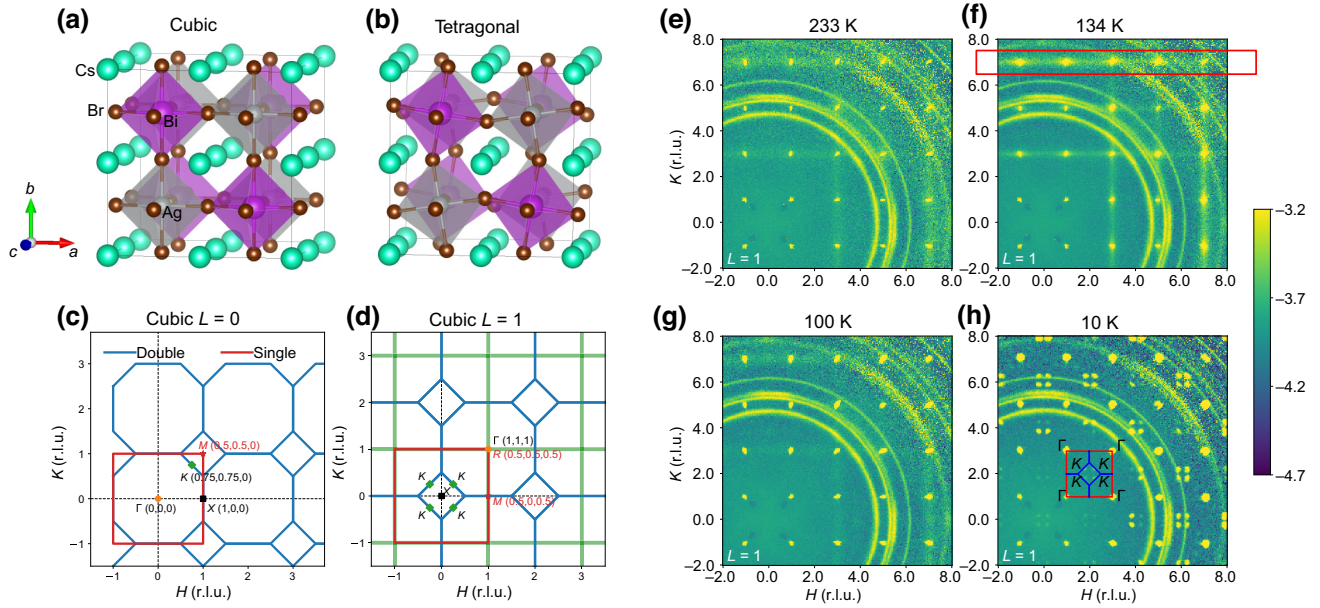
FIG. 1. $Cs_2AgBiBr_6$ crystal structures, Brillouin zones (BZ), and diffuse scattering. (a),(b) Structures of cubic and tetragonal $Cs_2AgBiBr_6$. Cs, Ag, Bi, and Br atoms are shown in cyan, silver, purple, and brown, respectively. The tetragonal rotation axis in (b) is the c axis. (c),(d) Projection of cubic structure BZ boundaries in (c) ($L = 0$) plane and (d) ($L = 1$) plane (in double perovskite conventional notation). Blue lines are the double-perovskite BZ boundaries, and red lines are the single perovskite BZ boundaries. Green lines symbolize the location of observed diffuse rods, connecting Γ and X points of the double perovskite BZ for (H, K, L) all odd, which corresponds to the BZ edges for the single perovskite notation. Green diamonds represent K points of double-perovskite BZ, which become superlattice peaks at low T. (e)–(h) Neutron diffuse scattering data measured in the reciprocal plane ($L = 1$) using CORELLI (E-discriminating cross-correlation turned off) at (e) $T = 233$ K, (f) 134 K, (g) 100 K, and (h) 10 K. The L-integration range is 0.96 to 1.04 (r.l.u.). The red rectangle in (e) highlights a diffuse rod. Red and blue lines in (h) mark the single-perovskite and double-perovskite BZ edges, respectively. Color maps in (e)–(h) use a $\log_{10}$ scale. Concentric rings in neutron data are from diffraction by polycrystalline aluminum and copper parts of the sample holder (absent from x-ray measurements).

energy-integrated data (CC off) than in the cross-correlated data (nearly elastic scattering), indicating that the rods have an inelastic component, although they also extend into the quasielastic regime, since the cross-correlation energy filtering is approximately 1 meV around the elastic channel Fig. 2(c). Recent neutron and x-ray scattering measurements on $CsPbBr_3$ revealed similar diffuse rods with an extended quasielastic component over $0 \leqslant E \leqslant 2$ meV, for transverse-acoustic (TA) modes dominated by Br motions along the edges of the simple perovskite BZ [30]. Our first-principles simulations pointed out their origin in the competition of in-phase versus out-of-phase patterns of collective $PbBr_6$ octahedra rotations corresponding to the lowest-energy TA phonons at the M and R points of the simple perovskite BZ [30]. A recent first-principles computational study [40] of electron-phonon coupling in several inorganic halide single-perovskites proposed a picture of strongly coupled optical vibrations and also found a strong damping of zone-boundary acoustic modes, matching our prior reports on $CsPbBr_3$ [30].

While the behavior observed in $Cs_2AgBiBr_6$ establishes a more general character in the MHP family of slow correlated fluctuations first observed in $CsPbBr_3$ [30], we also note important differences between the two compounds.

In particular, the intensity along diffuse rods in cubic $CsPbBr_3$ is clearly modulated with maxima at M and R points [30], whereas the rods in $Cs_2AgBiBr_6$ exhibit no local maximum at M (X point in double perovskite), and the R points correspond to the Ag/Bi ordering superlattice peaks (Γ points in double perovskite). The absence of maxima at M/X, can be related to the different types of transition into the tetragonal phase. The soft-mode condensation at Γ in the double-perovskite is a second-order transition and yields tetragonal symmetry without introducing superlattice peaks as the unit cell is unchanged. On the other hand, the M-point mode in $CsPbBr_3$ condenses at a first-order transition and doubles the unit cell. In addition, the diffuse rods remain strong in the tetragonal phase of $CsPbBr_3$, but become much weaker in tetragonal $Cs_2AgBiBr_6$. Upon cooling $Cs_2AgBiBr_6$ deeper in the tetragonal phase, the X point does not condense, but we show below how a low-lying mode near K points condenses instead [see Fig. 1(h)] and creates a more complex distorted ground-state structure than previously reported [22,24,63,64].

To investigate the phononic origin of the diffuse rods, and anharmonic renormalization in the cubic phase, we performed *ab initio* molecular dynamics (AIMD)
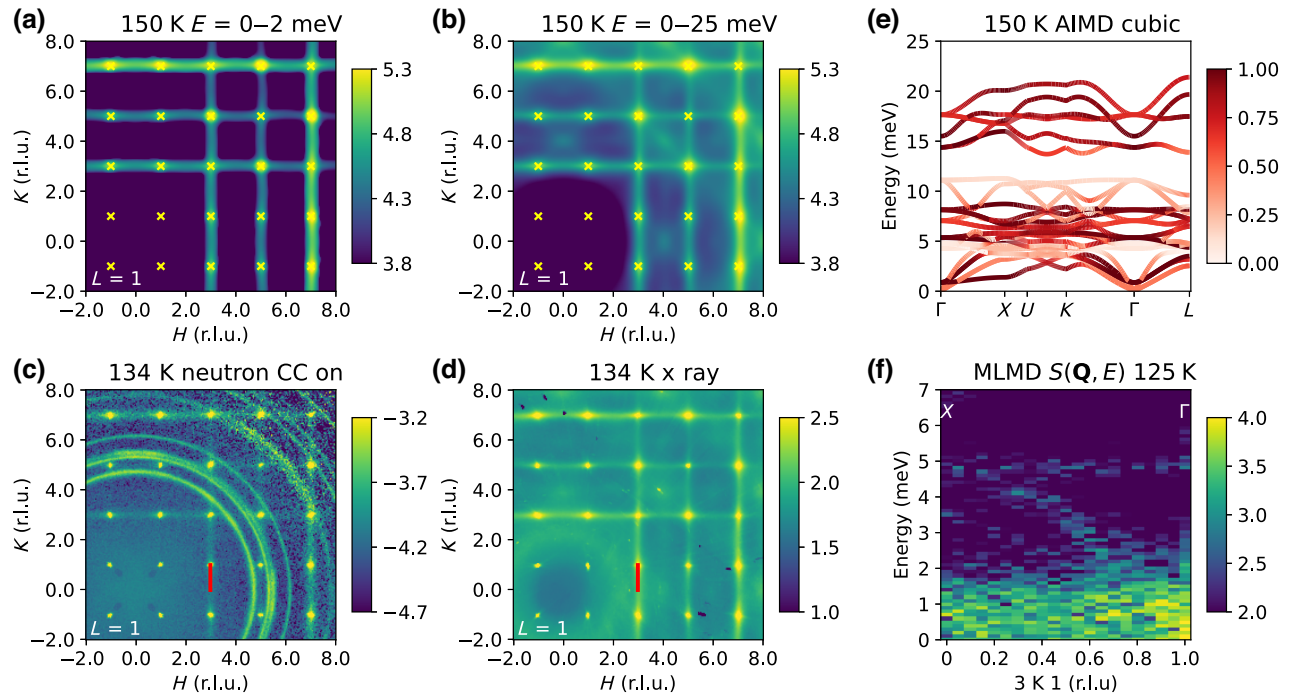
FIG. 2. Diffuse rods in cubic phase and damped low-energy optic branch. (a),(b) Thermal diffuse scattering (TDS) simulations for cubic phase computed using TDEP 150 K force-constants. Energy integration ranges 0–2 meV and 0–25 meV are shown in (a),(b) and compared with (c) neutron measurements at 134 K (with CC turned on) and (d) X-ray measurement at 134 K. In all TDS simulations, the location of Bragg peaks are indicated by yellow crosses. Panels (e) shows the Br eigenvector weighted phonon dispersions of 150 K cubic phase. The color maps on dispersions refer to the modulus of Br components in eigenvectors of each mode. As eigenvectors are normalized to one for each mode as $\sum_j e_j^2 = 1$, where j is atom and e_j is eigenvector, the minimum of color map is 0 and maximum is 1. (f) $S(\mathbf{Q}, E)$ along $(3, K, 1)$ calculated from 125 K MLMD trajectory on a $4 \times 20 \times 4$ supercell (12 800 atoms). The low-energy damped optic branch is responsible to the diffuse rods observed in neutron and X-ray experiment, as marked as red segments in (c),(d). Color maps in (a)–(d) are in $\log_{10}$ scale, while that of panel (e) is in linear scale. Concentric rings in neutron data are from diffraction by polycrystalline aluminum and copper parts of the sample holder (absent from X-ray measurements).

simulations at 300 and 150 K (cubic). The AIMD trajectories were used as input to the temperature-dependent effective potential (TDEP) method to obtain renormalized second-order force constants and associated phonon dispersions [67–69]. The renormalized phonon dispersions are shown in Fig. 2(e) and Fig. S18 within the Supplemental Material [66]. As seen on these plots, the $\Gamma - X$ branch is unstable in harmonic calculations but becomes anharmonically stabilized by thermal fluctuations, yielding a low-lying flat branch at $E \sim 1.5$ meV at 300 K, in good agreement with previous simulations [61], and with our INS measurements of phonon energies shown in Fig. 4. This branch is even softer at 150 than at 300 K and results in more intense thermal diffuse scattering (TDS) (Fig. S20 within the Supplemental Materials [66]), consistent with our measurements showing an increased rod intensity just above $T_{c1} \simeq 122$ K, since the TDS is proportional to the Bose-Einstein occupation factor and thus highly sensitive to low-energy phonons. We emphasize that the entire $\Gamma - X$ low-energy optic branch softens, instead of just the wave vector (Γ) of the soft mode corresponding to the

cubic-tetragonal transition. The lowest energy optic branch along $\Gamma - X$ is dominated by Br octahedra rotations, as revealed by the phonon dispersions weighted by Br motion amplitudes shown in Fig. 2(e) and by phonon animations in the Supplemental Material [66]. The Γ mode involves out-of-phase octahedra rotations like the R mode in the single perovskite, while the X mode involves in-phase rotations like the M mode in the single-perovskite. The dynamical structure factor, $S(\mathbf{Q}, E)$, was further computed using the renormalized force constants in the cubic phase [see Eq. (C1) and details in Appendix]. Results at 150 K are shown in Figs. 2(a) and 2(b). To compare with CORELLI data, the simulated $S(\mathbf{Q}, E)$ was integrated over $0 \leqslant E \leqslant 2$ meV (quasielastic channel) to compare with Fig. 2(c), or $0 \leqslant E \leqslant 25$ meV (full TDS corresponding to cross-correlation chopper off or to x-ray diffuse scattering) to compare with Fig. 2(d). The excellent agreement between the computed TDS and measured diffuse scattering maps, for both neutron and x-ray scattering, further establishes that the low-energy flat branch from Br motions is responsible for the diffuse rods observed in planes $L =$ odd. Due

to the phase factor, these rods have suppressed intensity in planes $L = $ even (Figs. S2 and S3 within the Supplemental Material [66]).

While our TDS simulations using renormalized force constants account for the observed diffuse scattering signal very well, the TDEP method still describes the system within an effective second-order harmonic approximation. To fully include the effect of anharmonicity on the phonon spectral functions, without the limitations of perturbation theory, we further used machine-learning-based molecular dynamics (MLMD), with a neural-network force field trained against AIMD data (see Appendix). Figure 2(f) shows the $S(\mathbf{Q}, E)$ along $[3, K, 1]$ calculated from the 125 K MLMD trajectory [$4 \times 20 \times 4$ supercell containing 12 800 atoms, see Eq. (D3) and details in the Appendix]. It clearly reveals the flat low-energy optic branch, which is strongly damped along the entire $\Gamma - X$ segment and results in a broad spectrum with quasielastic component $E \leqslant 2$ meV. This behavior is a signature of the strong anharmonic damping of Br octahedra rotations. The breakdown of these modes into very low-energy fluctuations is responsible for the strong diffuse rods along $\Gamma - X$, as indicated by the red segment along $[3, K, 1]$ marked in Figs. 2(c) and 2(d). In addition, we performed MLMD on a large $20 \times 20 \times 20$ supercell (320 000 atoms) to compute the diffuse scattering (see Appendix). MLMD simulations reproduce the observed diffuse rods, validating the training of the neural-network force field. As shown in the atomically decomposed diffuse scattering maps shown in Fig. 3 and Figs. S25–27 within the Supplemental Material [66], the diffuse rods in $(H, K, L = $ odd) planes are mostly contributed by Br atoms, while Ag and Bi result in all-odd integer Bragg peaks, consistent with the $Fm\bar{3}m$ symmetry (see Appendix D). We note that the anharmonic optic mode discussed herein is quite distinct from INS results in hybrid organic-inorganic halide single-perovskites reported in Ref. [70]. That study found multiple flat, nondispersive optic modes associated with the dynamics of the organic cations in a wide energy range (approximately 3–40 meV), which strongly broaden upon warming [70]. Importantly, that study did not report on the low-energy acoustic modes along $M - R$, nor on the anharmonic optic mode of the halide sublattice observed here in $Cs_2AgBiBr_6$.

B. Inelastic neutron scattering

We now compare our INS measurements with our phonon simulations and show that low-energy acoustic modes retain a sharp nature, contrasting strongly with the behavior of soft, broad optic phonons for Br octahedra rotations. We conducted high-resolution INS on $Cs_2AgBiBr_6$ single crystals using the cold neutron triple-axis spectrometer (CTAX) and HB-3 triple-axis spectrometer at the high-flux isotope reactor (details in
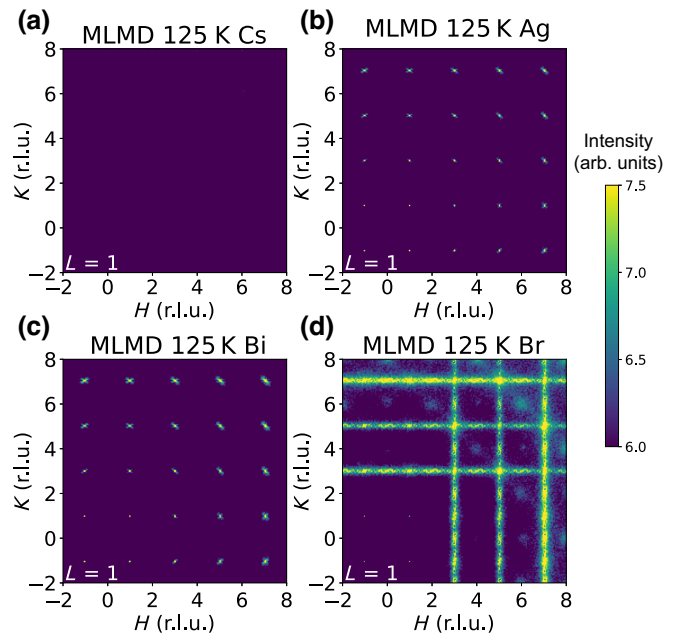

FIG. 3. Decomposition of diffuse scattering in $(H, K, L = 1)$ plane calculated from MLMD trajectories at 125 K using a $20 \times 20 \times 20$ supercell (320 000 atoms). Diffuse scattering from (a) Cs, (b) Ag, (c) Bi, and (d) Br elements.

Appendix). The TA phonons measured along $[4, K, 0]$ and $[-H, 4, -H]$ at 300 K are shown in Figs. 4(a) and 4(b). They exhibit clear peaks with relatively narrow linewidths. In contrast, the spectra at $\mathbf{Q} = (7, 1, 1)$ shown in Fig. 4(c), reveal that the low-energy zone-center optic mode is strongly broadened at 300 K, with only a broad bump at approximately 1.5 meV. Additional CTAX phonon spectra along $[0, 4 - K, 0]$, $[2 + H, 2 - H, 0]$ at 300 K, and at $(3, 1, 1)$ at several temperatures are shown in the Supplemental Material [66].

The INS spectra were fit with a damped harmonic oscillator (DHO) model convolved with the experimental resolution (details in the Supplemental Material [66]). The resulting phonon energies and linewidths are shown in Fig. 4(d). As can be seen, our computed renormalized phonon dispersions at 300 K agree very well with our 300-K INS measurements. In addition, a clear softening of the zone-center optic mode is observed at 135 K ($E = 0.70$ meV) compared to 300 K ($E = 1.44$ meV), confirming that the zone-center soft-mode condensation in the cubic phase yields the tetragonal transition [24,61,63]. The phonon spectra measured along $[4, K, 0]$ at 300 K are plotted as a color map in Fig. 4(e). The sharp nature of acoustic modes is captured well by our MLMD $S(\mathbf{Q}, E)$ simulations [Fig. 4(f) and Fig. S24 within the Supplemental Material [66]], which validates our neural-network force field, and strongly contrasts with the broad flat optic branch along $\Gamma - X$ shown in Fig. 2(f).
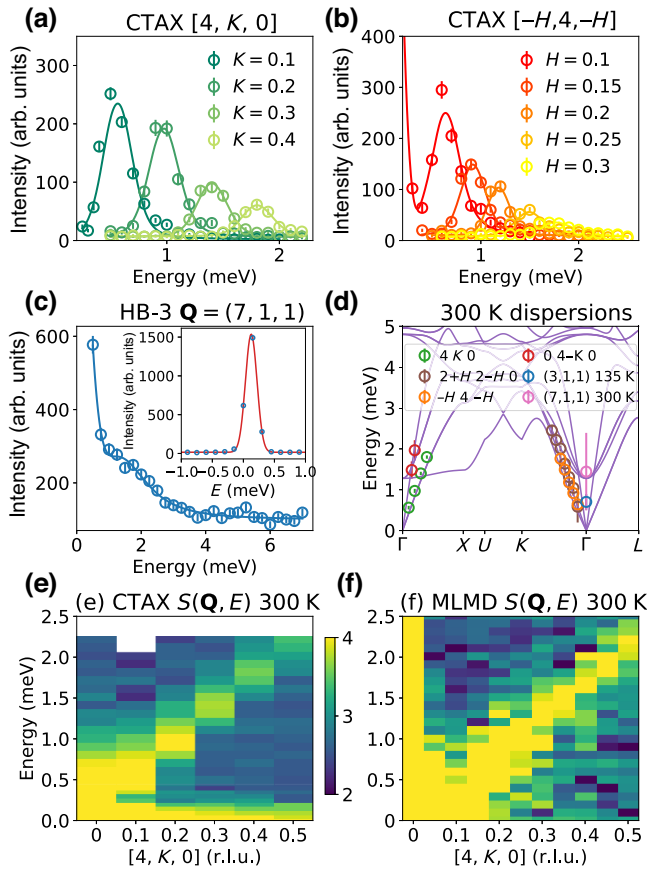
FIG. 4. Inelastic neutron-scattering spectra and phonon dispersions. (a),(b) CTAX measurements along at 300 K along (a) $[4, K, 0]$ and (b) $[-H, 4, -H]$. (c) HB-3 measurement at $\mathbf{Q} = (7, 1, 1)$ at 300 K. The scattered markers in (a)–(c) are measured data and lines are fitted curves using damped harmonic oscillator models convolving with instrumental resolutions. The inset plot in (c) shows the scan at $\mathbf{Q} = (7, 1, 1)$ across elastic line (markers). The fitted Gaussian curve (red lines) centered at energy 0.126 meV. This value is used to correct the phonon frequency at zone center. (d) Renormalized phonon dispersions using cubic phase 300 K AIMD force constants compared with experimental data. Markers are fitted phonon energies, and error bars indicate fitted intrinsic phonon linewidths. (e) $S(\mathbf{Q}, E)$ along $[4, K, 0]$ direction measured at CTAX, generated by stacking scans with different K, comparing with (f) MLMD calculated $S(\mathbf{Q}, E)$ on a $4 \times 20 \times 4$ supercell (12 800 atoms). The color maps of (e),(f) are in $\log_{10}$ scale.

C. Tetragonal phase instability and ground state

As discussed above, the tetragonal phase results from a modulation of the cubic structure by out-of-phase octahedral rotations, due to the soft zone-center optic mode. Indeed, distorting the cubic structure with the eigenvector of the zone-center mode resulted in a tetragonal structure with space group $I4/m$, whose parameters (Table S1 within the Supplemental Material) agree well with reported experimental values [24]. Further harmonic phonon simulations performed on this structure were stable across

most of the BZ, but surprisingly retained a weak instability near the K point, (0.75, 0.75, 0) in double-perovskite conventional notation, as shown in Fig. S13 within the Supplemental Material [66](b). The eigenvector of this unstable mode mainly involves Br and Cs motions and is illustrated in Supplemental Material [66] animations. This phonon instability indicates that the true ground state should exhibit a further distortion and enlarged unit cell. Indeed, the unstable mode matches well the wave vectors of the superlattice peaks observed in the CORELLI measurements at 10 K, see Fig. 1(h) and low-T x-ray data in Figs. 5(b) and 5(c) (see Ref. [71]). However, we note that superlattice peaks appear slightly away from K, closer to (0.8, 0.8, 0) and are possibly incommensurate. Since the imaginary phonon frequency of the computed soft-mode at K is small, the instability is weak and the phase transition occurs at low temperature. As expected, this instability is sensitive to the exchange-correlation functionals and the unit cell volume (Fig. S15 within the Supplemental Material [66]). Barely unstable dispersions were obtained by interpolating force constants (FCs) at different volumes [Fig. 5(d) and Fig. S16 within the Supplemental Material [66]], and subsequently were used to compute $S(\mathbf{Q}, E)$, integrated over $0 \leqslant E \leqslant 25$ meV to obtain the TDS in Fig. 5(a). This can directly be compared with the 30 K x-ray diffuse scattering in Fig. 5(b), showing excellent agreement. We note that K points are close to the X points in the BZ [Figs. 2(c) and 2(d)] and share some similarities in their eigenvectors. Both of the low-energy modes at K and X introduce in-phase octahedral rotations. However, within $a - b$ layers, instead of having a two single-perovskite periodicity, the soft mode near K modulates the rotation with a larger wavelength. As shown in Fig. 5(f), the modulation by the eigenvector of mode at (0.8, 0.8, 0) results in a large $5 \times 5 \times 1$ supercell of the original double-perovskite cell, containing 1000 atoms (distortion amplitude exaggerated to help visualize atomic displacements). We see that in addition to Br displacements mainly in the a-b plane, Cs displacements occur along the c axis. The modulation resulting from the incommensurate soft mode near K reduces the symmetry of the tetragonal structure. Our DFT simulations suggest that the ground state could have space-group Pm (no. 6) with a $4 \times 4 \times 1$ supercell (640 atoms) as modulated by wave vector (0.75, 0.75, 0), although the monoclinic distortion angle away from $90°$ could be very small. If a modulation wave vector of (0.8, 0.8, 0) is used instead, an even larger $5 \times 5 \times 1$ supercell (1000 atoms) results, with a possible space group Cm (no. 8) (see details in Sec. VIII within the Supplemental Material [66]). We note that distortion energies are exceedingly small (less than 0.1 meV/atom) and thus sensitive to details of the DFT simulations.

In addition, our low-T x-ray measurements clearly show a broad diffuse intensity maximum at X points at 134 K (cubic phase) and strengthening at 100 K (tetragonal)
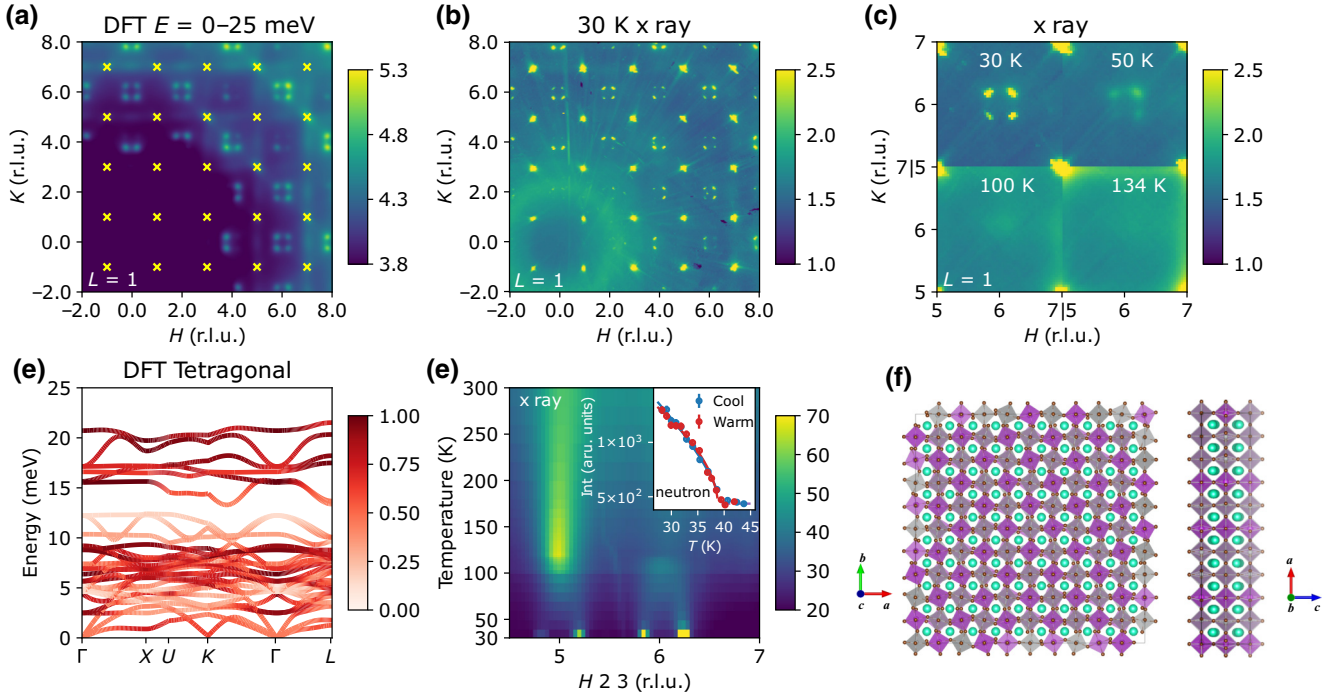
FIG. 5.   Lattice instability of tetragonal phase at K points and modulated ground state. (a) TDS simulation in tetragonal phase (plane $L = 1$) integrated over the energy range 0–25 meV, computed using interpolated harmonic DFT force constants. The location of Bragg peaks is indicated by yellow crosses. (b) Experimental x-ray data (plane $L = 1$) measured at 30 K, and enlarged portion in (c) comparing data at 30, 50, 100, and 134 K. As seen in (c), X-point intensity gradually splits to four nearby K points. (d) Phonon dispersions of harmonic DFT tetragonal phase, with color coding indicating the modulus of Br eigenvector. Eigenvectors are normalized to unity for each mode as $\sum_j e_j^2 = 1$, where j is atom and e_j is eigenvector, the minimum of the color map is 0 and maximum is 1. (e) Waterfall plot of x-ray scattering intensity along $[H, 2, 3]$ (r.l.u) over a large temperature range. The X points at $(5, 2, 3)$, $(6, 2, 3)$ start to split approximately 122 K on cooling, indicating cubic-tetragonal phase transition. The background discontinuity approximately 90 K is due to the change from helium to nitrogen cooling gas, while the sudden increase of intensity below 40 K indicates the phase transition from soft modes near K-point condensing. (f) Predicted exaggerated ground-state structure viewed along c and b axis. The color maps of (a)–(c) are in $\log_{10}$ scale, while (d),(e) are in linear scale.

and gradually splitting into sharper maxima close to K points, eventually condensing into intense superstructure Bragg spots [Figs. 5(b) and 5(c)]. A gradual temperature evolution is revealed in Fig. 5(e), which shows the intensity along $(H, 2, 3)$ from 300 to 30 K. Cooling below $T_{c1} = 122$ K, each X-point maximum ($H = \{5, 6\}$) splits into two maxima around K points ($H = \{4.75, 5.25\}$ and $\{5.75, 6.25\}$ respectively). Note that the path in Fig. 5(e) is integrated over a wide band to include K points at $(H, 2, 3 \pm 0.25)$. A clear increase in intensity near K occurs below 40 K, indicating the transition to the distorted ground state. This is entirely consistent with the condensation of the soft mode near K and its competition with the X point near instability (see discussion in Secs. VI and VII within the Supplemental Material [66]). Using CTAX, we tracked the superlattice peak intensity over a cooling and warming cycle (details in Sec. VII within the Supplemental Material [66]), as shown in the inset of Fig. 5(e). The intensity was fit to $A \cdot (T_{c2} - T)^x + b$, where A, T_{c2}, x and b are parameters and T is temperature. The fit results for T_{c2} from cooling and warming curves are 39.36 ± 0.34

and 38.78 ± 0.20 K, respectively. The coincidence of cooling and warming curves and T_{c2} values supports that this phase transition is of second order (or weak first order), and originates from the condensation of a soft mode near the K point. We note that during paper preparation, a phase transition at $T \sim 38$ K was reported based on Raman spectroscopy, supporting our findings, although that Raman study did not discuss the ground-state structure or soft-mode wave vector [62]. Further, the minute change in dielectric constant across $T \sim 38$ K appears to rule out a polar point-group symmetry of the ground state [62], incompatible with Pm or Cm. This could reflect a tiny polarization or the incommensurable nature of the distortion, only approximated here based on eigenvectors at commensurate wave vectors.

III. CONCLUSION

In summary, we reported the first momentum-resolved investigations of complex dynamic fluctuations in the double-perovskite $Cs_2AgBiBr_6$ based on single-crystal

neutron and x-ray scattering measurements, rationalized with first-principles simulations augmented with large-scale machine-learning models. We revealed the occurrence of systematic diffuse scattering rods arising from slow, correlated 2D fluctuations of Br octahedra derived from strongly anharmonic low-energy optic phonons. While arising from low-energy optic phonon branches, these large fluctuations share similarities with the overdamped zone-boundary acoustic modes in the single-perovskite $CsPbBr_3$, reflecting the phonon band folding in the double-perovskite unit cell. The present results therefore suggest a general behavior of slow correlated 2D fluctuations of the inorganic framework in metal bromide perovskites. Since the electronic states at the edges of the band gap are derived from hybridized metal and halide orbitals, the structural fluctuations of metal-halide octahedra are likely significant to understand the electron-phonon coupling properties and thermalization process of photoexcited carriers in photovoltaic applications.

Further, our experimental observations directly reveal how specific phonon modes are strongly anharmonic and temperature dependent, which sheds light on the origin of the ultralow thermal conductivity that enables $Cs_2AgBiBr_6$ as a candidate thermoelectric material. Importantly, our diffraction measurements enabled the observation of a new structural phase transition to a low-symmetry phase at $T \leqslant T_{c2} = 39$ K. We further rationalize the transition in terms of a phonon instability of the tetragonal phase near the K point, resulting in an unusually complex ground state with several hundred atoms in the unit cell.

Extending our previous findings in $CsPbBr_3$, our results suggest ubiquitous lattice instabilities in the halide-perovskite family resulting from their anharmonic potential energy surface, and reveal a much more complex ground state than previously known in $Cs_2AgBiBr_6$. The complex anharmonic lattice dynamics yield large thermal fluctuations and strongly impact the phonon-phonon and electron-phonon coupling and thus the thermal and optoelectronic properties, which are of direct relevance to a number of energy applications of metal-halide perovskites, spanning photovoltaics and thermoelectrics.

APPENDIX A: SAMPLE SYNTHESIS

48% w/w aq. hydrobromic acid (HBr) and bismuth (III) bromide ($BiBr_3$) (metals basis) with purity of 99% were purchased from Alfa Aesar, and silver bromide (AgBr) (metals basis) with purity of 99% and cesium bromide (CsBr) with 99.9% purity were purchased from Sigma Aldrich. All the chemicals were directly used as received without any further purification process. Briefly, $Cs_2AgBiBr_6$ was synthesized through a solution-processed method with some modification [21]. 4.85 g CsBr, 2.15 g AgBr, and 5.11 g $BiBr_3$ were dissolved into 125 ml HBr solution in a sealed container at 120 °C on a hot plate after about 2-h stirring. The precursor solution was filtered at 120 °C before single-crystal growth. Finally, large single crystals can be grown by gradually reducing the heating temperature of hot plate to 80 °C at a rate of 0.5 °C/h. To avoid any light-induced chemicals decomposition, the $Cs_2AgBiBr_6$ single crystals were grown in the dark condition. A photograph of a $Cs_2AgBiBr_6$ single crystal is shown in Supplemental Material [66].

APPENDIX B: X-RAY AND NEUTRON SCATTERING

1. Diffuse x-ray scattering

Diffuse x-ray scattering data were collected at the Advanced Photon Source on sector 6-ID-D using an incident energy of 87.0 keV. Sample temperatures from 30 to 300 K were controlled with He and N_2 gas flow. During the measurements, the samples were continuously rotated about an axis perpendicular to the beam at $1° \text{ s}^{-1}$ over 370°, with images recorded every 0.1 s on a Dectris Pilatus 2M detector with a 1-mm-thick CdTe sensor layer. Three sets of rotation images were collected for each

sample at each temperature to fill in gaps between the detector chips. The resulting images were stacked into a three-dimensional array, oriented using an automated peak search algorithm and transformed in reciprocal space coordinates, allowing $S(\mathbf{Q})$ to be determined over a range of approximately ± 15 Å^{-1} in all directions. The x-ray scattering intensities are proportional to $S(\mathbf{Q})$, weighted by the square of the atomic scattering factors for each element. Further details are given in Ref. [72].

2. Diffuse neutron scattering

Neutron diffuse scattering experiments were conducted using the CORELLI instrument at SNS, Oak Ridge National Laboratory (ORNL) as a function of temperature. Unlike conventional single-crystal x-ray or neutron diffractometers, CORELLI uses a wide wavelength band to cover large swaths of wave vectors $\mathbf{Q}$ in reciprocal space, but enables the discrimination of quasielastic versus inelastic signals with a resolution of approximately 1 meV, through the use of a semirandom chopper and cross-correlation technique. The crystal was mounted on an aluminum pin with thin copper wire, with the pin wrapped in Gd foil to reduce background, and the assembly was loaded on closed-cycle refrigerator. Measurements were performed on cooling down to $T \sim 10$ K as well as warming to approximately 400 K. At selected temperatures, the sample was rotated over a wide range of angle ($360°$) to collect large continuous data volumes in reciprocal space and investigate the diffuse scattering.

3. Inelastic neutron scattering

Inelastic neutron scattering (INS) measurements were conducted on the Cold Neutron Triple-Axis Spectrometer (CTAX) and HB-3 triple-axis spectrometer at the High Flux Isotope Reactor (HFIR), ORNL. A few single crystals of $Cs_2AgBiBr_6$ were used with mass $0.2 \sim 0.4$ g. Samples had mosaics of about $30'$. Using CTAX, we measured acoustic modes along $[4, K, 0]$ at 300 and 100 K, $[-H, 4, -H]$ at 300 K, $[0, 4-K, 0]$ at 300 K, $[2+H, 2-H, 0]$ at 300 K, and optic mode at $\mathbf{Q} = (3, 1, 1)$ at 550, 300, and 135 K. Using HB-3, we measured the lowest optic mode at $\mathbf{Q} = (7, 1, 1)$ at 300 K.

In CTAX experiments, the fixed final energy mode was used with $E_f = 5$ meV for measurement along $[4, K, 0]$ at 300 and 100 K, and with $E_f = 4.8$ meV for measurements along $[-H, 4, -H]$ at 300 K, $[0, 4-K, 0]$ at 300 K, $[2+H, 2-H, 0]$ at 300 K and $\mathbf{Q} = (3, 1, 1)$ at 550, 330, and 135 K. PG002 monochromators and analyzers were used. The collimation settings were $30'$-$100'$ $80' - 120'$, and energy resolution was approximately 0.3 meV at zero energy transfer. The high-order energy contamination of neutron beam was removed by a cooled Be filter. Samples were mounted in the $(H, K, 0)$ plane using Bragg peaks $(4, 0, 0)$ and $(0, 4, 0)$ for measurements

along $[4, K, 0]$ and $[2+H, 2-H, 0]$. The scattering plane $(3H, K, H)$ defined by $(3, -1, 1)$ and $(3, 1, 1)$ was used for measurements at $\mathbf{Q} = (3, 1, 1)$, along $[-H, 4, -H]$, and $[0, 4-K, 0]$. While $[-H, 4, -H]$ is not within the $(3H, K, H)$ scattering plane, the required tilts were reachable with the instrument goniometer. We note that $[4, K, 0]$ and $[0, 4-K, 0]$ both correspond to wave vectors along $\langle 001 \rangle$, and are TA modes and longitudinal acoustic (LA) modes from Γ to X, respectively. Along $[2+H, 2-H, 0]$ and $[-H, 4, -H]$, we probe the two nondegenerate TA modes from Γ to K, which have distinct polarizations.

In the HB-3 experiment, the fixed final energy mode was used with $E_f = 13.5$ meV. PG002 monochromators and analyzers were used. The collimation setting was $30' - 40' - 40' - 70'$, and the energy resolution was approximately 1 meV at zero energy transfer. The sample was mounted in the $(H, K, 0)$ plane. $\mathbf{Q} = (7, 1, 1)$ was reached with tilts of the instrument goniometer.

APPENDIX C: FIRST-PRINCIPLES SIMULATIONS

First-principles phonon simulations were performed using VASP [73–76] in the cubic and tetragonal phases of $Cs_2AgBiBr_6$, with a special attention paid to anharmonic effects. We first describe the results of phonon simulations within the small-displacement approach and the harmonic approximation, as implemented in Phonopy [77], in the cubic phase ($Fm\overline{3}m$, space group 225), using a $2 \times 2 \times 2$ supercell of the double-perovskite cell with experimental lattice constant 11.2695 Å from Ref. [78] (details in the Supplemental Material [66]). These harmonic simulations result in unstable phonon dispersions, as shown in Fig. S13 and Fig. S14 within the Supplemental Material [66]. The unstable mode at the Γ point is triple degenerate, corresponding to out-of-phase rotations of Br octahedra about the three $\langle 100 \rangle_{cubic}$ axes. Modulating the cubic structure according to the eigenvector of one of these unstable modes results in the tetragonal structure. The structure was then relaxed using VASP until the force on each atom was smaller than 10^{-4} eV/Å, yielding the expected $I4/m$ symmetry (space group number 87), see details within the Supplemental Material [66]. The relaxed structure has lattice constants $a = b = 11.162$ Å, $c = 11.488$ Å, which compare well with experimental values $a = 7.8794 \times \sqrt{2} = 11.143$ Å, $c = 11.324$ Å [24]. After relaxing the tetragonal structure, further harmonic phonon simulations were performed. The phonon dispersions were then nearly stable, with only a weak instability around the K point [(0.75,0.75,0) in double perovskite conventional notation] as shown in Fig. S13 within the Supplemental Material [66]. This instability indicates that the true ground state exhibits a further modulated distortion and enlarged unit cell. Indeed, the location of the instability around K matches well the wave vectors of the superlattice peaks observed in the neutron and x-ray

diffuse scattering measurements below 40 K. Since the imaginary phonon frequency around this K-point mode is small, the instability is weak and the phase transition happens at low temperature, below 40 K. To investigate anharmonic effects at finite temperatures, we conducted *ab initio* molecular dynamics (AIMD) for the cubic phase at 300 and 150 K, and the tetragonal phase at 100 K. The AIMD were performed with VASP [73–76]. Subsequently, the temperature-dependent effective potential (TDEP) method [67–69] was used to extract renormalized effective second-order force constants. Further details are provided in Sec. IV within the Supplemental Material [66]. We also performed AIMD and extended MD simulations with a machine-learned force field, as described in the next section.

The dynamical structure factor $S(\mathbf{Q}, E)$ was computed for the cubic and tetragonal phases using either the harmonic or renormalized force constants to obtain phonon frequencies ω_s and eigenvectors e_{ds}. The simulated phonon intensity was calculated as [79]

$$S(\mathbf{Q}, E) \propto \sum_{s,\tau} \frac{1}{\omega_s} \left| \sum_d \frac{\overline{b_d}}{\sqrt{M_d}} \exp(-W_d)\exp(\mathrm{i}\mathbf{Q}\cdot\mathbf{d})(\mathbf{Q}\cdot\mathbf{e}_{ds}) \right|^2$$
$$\times \langle n_s + 1\rangle \delta(\omega - \omega_s)\delta(\mathbf{Q} - \mathbf{q} - \tau), \qquad \text{(C1)}$$

where $\overline{b_d}$ is neutron scattering length of atom d, $\mathbf{Q} = \mathbf{k} - \mathbf{k}'$ is the wave-vector transfer, and $\mathbf{k}'$ and $\mathbf{k}$ are the final and incident wave vector of the scattered particle, $\mathbf{q}$ the phonon wave vector, ω_s the eigenvalue of the phonon corresponding to the branch index s, τ is the reciprocal lattice vector, d the atom index in the unit cell, $\exp(-2W_d)$ the corresponding Debye-Waller factor, and $n_s = [\exp(\hbar\omega_s/k_\mathrm{B}T) - 1]^{-1}$ is the mean Bose-Einstein occupation factor. The phonon eigenvalues and eigenvectors in Eq. (C1) were obtained by solving dynamical matrix using Phonopy [77]. The thermal diffuse scattering (TDS) signals are obtained by integrating $S(\mathbf{Q}, E)$ over energy.

APPENDIX D: MACHINE-LEARNING AUGMENTED MOLECULAR DYNAMICS (MLMD)

We have extended the molecular dynamics simulation to a larger scale to access the well-resolved dynamics in $(\mathbf{Q}, E)$ space using a machine-learned force field (MLFF) based on a neural-network potential. To generate a force field that describes the dynamics over a broad temperature range, we generated AIMD training datasets over a range of temperatures using VASP [73–76]. These simulations were performed with the strongly constrained and appropriately normalized (SCAN) exchange-correlation functional [80]. We performed AIMD on a 40-atom unit cell, with a plane-wave kinetic energy cutoff of 400 eV and a $2 \times 2 \times 2$ Monkhorst-Pack grid of k points [81]. The

self-consistent convergence threshold for electronic minimization was set to 10^{-6} eV. We ran simulations from 100 to 900 K in 100-K intervals, with each trajectory lasting about 3–5 ps and a time step of 2 fs. All AIMD simulations used the 300-K experimental lattice constant 11.27 Å [24]. The temperature of the system was controlled by a Nosé-Hoover thermostat. We then used the DEEPMD [82] code to generate a MLFF based on a neural network, which reproduces as best as possible the AIMD dynamics. The generated MLFF was used to compute the pair distribution function and mean-squared displacements and checked against AIMD results. The LAMMPS package was then used for MLMD classical simulations with the trained MLFF [83]. We calculated the $S(\mathbf{Q}, E)$ from MLMD trajectories at 125 and 300 K along $[4, K, 0]$ and $[3, K, 1]$. For these simulations, we used large supercells ($4 \times 20 \times 4$ supercell containing 12 800 atoms), and computed the atomic trajectories up to approximately 100 ps (with a time step of 1 fs) within an NVT ensemble. The simulation at 125 and 300 K used experimental lattice constants 11.23 and 11.27 Å, respectively [24]. These extensive simulations provide momentum and energy resolutions of approximately 0.1 Å^{-1} and approximately 0.1 meV, respectively, enabling us to resolve the dispersions. In neutron scattering experiments, the scattering intensity has contributions from both the coherent dynamical structure factor ($S_{\mathrm{coh}}^{IJ}(\mathbf{Q}, E)$) attributed to correlated dynamics between I^{th} and J^{th} element, and incoherent dynamical structure factor ($S_{\mathrm{inc}}^{I}(\mathbf{Q}, E)$) from uncorrelated self dynamics of the Ith element, respectively, defined as

$$S_{\mathrm{coh}}^{IJ}(\mathbf{Q}, E) = \frac{1}{2\pi} \int_0^\infty \sum_{i,j} e^{-i\mathbf{Q}\cdot(R_i^I(0) - R_j^J(t))} e^{iEt/\hbar} dt, \quad \text{(D1)}$$

$$S_{\mathrm{inc}}^{I}(\mathbf{Q}, E) = \frac{1}{2\pi} \int_0^\infty \sum_{i} e^{-i\mathbf{Q}\cdot(R_i^I(0) - R_i^I(t))} e^{iEt/\hbar} dt, \quad \text{(D2)}$$

where $R_i^I(t)$ is the ith atom position of element type I at time t, and the summation indices i and j represent the sum over Ith and Jth kind of elements in the simulation cell. The total measured neutron scattering intensity is then proportional to

$$S_{\mathrm{tot}}(\mathbf{Q}, E) \propto \sum_{I,J} b_{\mathrm{coh}}^I b_{\mathrm{coh}}^J S_{\mathrm{coh}}^{IJ}(\mathbf{Q}, E)$$
$$+ \sum_{J} (b_{\mathrm{inc}}^J)^2 \, S_{\mathrm{inc}}^J(\mathbf{Q}, E), \qquad \text{(D3)}$$

where b_{coh}^I and b_{inc}^I are the coherent and incoherent scattering length of Ith element and summation index I and J runs over different elements in the unit cell.

Diffuse scattering intensity calculations were performed with MLMD using a $20 \times 20 \times 20$ supercell containing

320 000 atoms. We ran MLMD simulations at 125 and 300 K with durations of about 20 ps with 2-fs time steps. We computed the total scattering intensity, $S(\mathbf{Q})$ at 1-ps interval (20 configurations) according to

$$S(\mathbf{Q}) \propto \int_0^\infty |\sum_I b_{\text{coh}}^I \sum_{i \in I} e^{-i\mathbf{Q} \cdot R_i(t)}|^2 dt, \qquad \text{(D4)}$$

where i is an index running over all atoms of type I, and b_{coh}^I is the coherent neutron-scattering length of atom type I. The diffuse scattering intensity of pair $I - I$ is defined as

$$S^{I-I}(\mathbf{Q}) \propto (b_{\text{coh}}^I)^2 \int_0^\infty |\sum_{i \in I} e^{-i\mathbf{Q} \cdot R_i(t)}|^2 dt, \qquad \text{(D5)}$$

where index i enumerates atoms of element type I. Note $S(\mathbf{Q}) \neq \sum_I S^{I-I}(\mathbf{Q})$.

The $S(\mathbf{Q})$ and $S^{I-I}(\mathbf{Q})$ computed at different time points were then averaged to obtain the diffuse scattering pattern.

---

[1] J. Huang, Y. Yuan, Y. Shao, and Y. Yan, Understanding the physical properties of hybrid perovskites for photovoltaic applications, Nat. Rev. Mater. **2**, 1 (2017).

[2] H. J. Snaith, Present status and future prospects of perovskite photovoltaics, Nat. Mater. **17**, 372 (2018).

[3] C. C. Stoumpos, C. D. Malliakas, J. A. Peters, Z. Liu, M. Sebastian, J. Im, T. C. Chasapis, A. C. Wibowo, D. Y. Chung, and A. J. Freeman, *et al.*, Crystal growth of the perovskite semiconductor CsPbBr$_3$: a new material for high-energy radiation detection, Cryst. Growth Des. **13**, 2722 (2013).

[4] Y. He, L. Matei, H. J. Jung, K. M. McCall, M. Chen, C. C. Stoumpos, Z. Liu, J. A. Peters, D. Y. Chung, and B. W. Wessels, *et al.*, High spectral resolution of gamma-rays at room temperature by perovskite CsPbBr$_3$ single crystals, Nat. Commun. **9**, 1609 (2018).

[5] L. Yin, H. Wu, W. Pan, B. Yang, P. Li, J. Luo, G. Niu, and J. Tang, Controlled cooling for synthesis of Cs$_2$AgBiBr$_6$ single crystals and its application for x-ray detection, Adv. Opt. Mater. **7**, 1900491 (2019).

[6] W. Lee, H. Li, A. B. Wong, D. Zhang, M. Lai, Y. Yu, Q. Kong, E. Lin, J. J. Urban, and J. C. Grossman, *et al.*, Ultralow thermal conductivity in all-inorganic halide perovskites, Proc. Natl. Acad. Sci. **114**, 8693 (2017).

[7] H. Xie, S. Hao, J. Bao, T. J. Slade, G. J. Snyder, C. Wolverton, and M. G. Kanatzidis, All-inorganic halide perovskites as potential thermoelectric materials: Dynamic cation off-centering induces ultralow thermal conductivity, J. Am. Chem. Soc. **142**, 9553 (2020).

[8] W. Ning, X.-G. Zhao, J. Klarbring, S. Bai, F. Ji, F. Wang, S. I. Simak, Y. Tao, X.-M. Ren, L. Zhang, W. Huang, I. A. Abrikosov, and F. Gao, Thermochromic lead-free halide double perovskites, Adv. Funct. Mater. **29**, 1807375 (2019).

[9] N. J. Jeon, H. Na, E. H. Jung, T.-Y. Yang, Y. G. Lee, G. Kim, H.-W. Shin, S. I. Seok, J. Lee, and J. Seo, A fluorene-terminated hole-transporting material for highly efficient and stable perovskite solar cells, Nat. Energy **3**, 682 (2018).

[10] Q. Jiang, Y. Zhao, X. Zhang, X. Yang, Y. Chen, Z. Chu, Q. Ye, X. Li, Z. Yin, and J. You, Surface passivation of perovskite film for efficient solar cells, Nat. Photonics **13**, 460 (2019).

[11] L. M. Herz, How lattice dynamics moderate the electronic properties of metal-halide perovskites, J. Phys. Chem. Lett. **9**, 6853 (2018).

[12] G. Xing, N. Mathews, S. Sun, S. S. Lim, Y. M. Lam, M. Grätzel, S. Mhaisalkar, and T. C. Sum, Long-range balanced electron- and hole-transport lengths in organic-inorganic CH$_3$NH$_3$PbI$_3$, Science **342**, 344 (2013).

[13] L. D. Whalley, J. M. Frost, Y.-K. Jung, and A. Walsh, Perspective: Theory and simulation of hybrid halide perovskites, J. Chem. Phys. **146**, 220901 (2017).

[14] R. L. Z. Hoye, L. Eyre, F. Wei, F. Brivio, A. Sadhanala, S. Sun, W. Li, K. H. L. Zhang, J. L. MacManus-Driscoll, P. D. Bristowe, R. H. Friend, A. K. Cheetham, and F. Deschler, Fundamental carrier lifetime exceeding 1 μs in Cs$_2$AgBiBr$_6$ double perovskite, Adv. Mater. Interfaces **5**, 1800464 (2018).

[15] B. Chen, P. N. Rudd, S. Yang, Y. Yuan, and J. Huang, Imperfections and their passivation in halide perovskite solar cells, Chem. Soc. Rev. **48**, 3842 (2019).

[16] H. Wei and J. Huang, Halide lead perovskites for ionizing radiation detection, Nat. Commun. **10**, 1 (2019).

[17] J. Li, Q. Yu, Y. He, C. C. Stoumpos, G. Niu, G. G. Trimarchi, H. Guo, G. Dong, D. Wang, and L. Wang, *et al.*, Cs$_2$PbI$_2$Cl$_2$, all-inorganic two-dimensional Ruddlesden–Popper mixed halide perovskite with optoelectronic response, J. Am. Chem. Soc. **140**, 11085 (2018).

[18] Y. He, M. Petryk, Z. Liu, D. G. Chica, I. Hadar, C. Leak, W. Ke, I. Spanopoulos, W. Lin, and D. Y. Chung, *et al.*, CsPbBr$_3$ perovskite detectors with 1.4% energy resolution for high-energy γ-rays, Nat. Photonics **15**, 36 (2021).

[19] X. Zhang, M. E. Turiansky, and C. G. Van de Walle, All-inorganic halide perovskites as candidates for efficient solar cells, Cell Rep. Phys. Sci. **2**, 100604 (2021).

[20] H. Lei, D. Hardy, and F. Gao, Lead-free double perovskite Cs$_2$AgBiBr$_6$: fundamentals, applications, and perspectives, Adv. Funct. Mater. **31**, 2105898 (2021).

[21] A. H. Slavney, T. Hu, A. M. Lindenberg, and H. I. Karunadasa, A bismuth-halide double perovskite with long carrier recombination lifetime for photovoltaic applications, J. Am. Chem. Soc. **138**, 2138 (2016).

[22] E. T. McClure, M. R. Ball, W. Windl, and P. M. Woodward, Cs$_2$AgBiX_6 ($X = $ Br, Cl): New visible light absorbing, lead-free halide perovskite semiconductors, Chem. Mater. **28**, 1348 (2016).

[23] J. Luo, *et al.*, Efficient and stable emission of warm-white light from lead-free halide double perovskites, Nature **563**, 541 (2018).

[24] L. Schade, A. D. Wright, R. D. Johnson, M. Dollmann, B. Wenger, P. K. Nayak, D. Prabhakaran, L. M. Herz, R. Nicholas, H. J. Snaith, and P. G. Radaelli, Structural and optical properties of Cs$_2$AgBiBr$_6$ double perovskite, ACS Energy Lett. **4**, 299 (2019).

[25] M. R. Filip, S. Hillman, A. A. Haghighirad, H. J. Snaith, and F. Giustino, Band gaps of the lead-free halide double perovskites $Cs_2BiAgCl_6$ and $Cs_2BiAgBr_6$ from theory and experiment, J. Phys. Chem. Lett. **7**, 2579 (2016).

[26] S. Zelewski, J. Urban, A. Surrente, D. Maude, A. Kuc, L. Schade, R. Johnson, M. Dollmann, P. Nayak, and H. Snaith, *et al.*, Revealing the nature of photoluminescence emission in the metal-halide double perovskite $Cs_2AgBiBr_6$, J. Mater. Chem. C **7**, 8350 (2019).

[27] O. Yaffe, Y. Guo, L. Z. Tan, D. A. Egger, T. Hull, C. C. Stoumpos, F. Zheng, T. F. Heinz, L. Kronik, and M. G. Kanatzidis, *et al.*, Local polar fluctuations in lead halide perovskite crystals, Phys. Rev. Lett. **118**, 136001 (2017).

[28] C. Gehrmann and D. A. Egger, Dynamic shortening of disorder potentials in anharmonic halide perovskites, Nat. Commun. **10**, 1 (2019).

[29] W. Li, A. S. Vasenko, J. Tang, and O. V. Prezhdo, Anharmonicity extends carrier lifetimes in lead halide perovskites at elevated temperatures, J. Phys. Chem. Lett. **10**, 6219 (2019).

[30] T. Lanigan-Atkins, X. He, M. Krogstad, D. Pajerowski, D. Abernathy, G. N. Xu, Z. Xu, D.-Y. Chung, M. Kanatzidis, and S. Rosenkranz, *et al.*, Two-dimensional overdamped fluctuations of the soft perovskite lattice in $CsPbBr_3$, Nat. Mater. **20**, 977 (2021).

[31] R. X. Yang, J. M. Skelton, E. L. Da Silva, J. M. Frost, and A. Walsh, Spontaneous octahedral tilting in the cubic inorganic cesium halide perovskites $CsSnX_3$ and $CsPbX_3$ $(X = F, Cl, Br, I)$, J. Phys. Chem. Lett. **8**, 4720 (2017).

[32] A. Marronnier, H. Lee, B. Geffroy, J. Even, Y. Bonnassieux, and G. Roma, Structural instabilities related to highly anharmonic phonons in halide perovskites, J. Phys. Chem. Lett. **8**, 2659 (2017).

[33] A. Marronnier, G. Roma, S. Boyer-Richard, L. Pedesseau, J.-M. Jancu, Y. Bonnassieux, C. Katan, C. C. Stoumpos, M. G. Kanatzidis, and J. Even, Anharmonicity and disorder in the black phases of cesium lead iodide used for stable inorganic perovskite solar cells, ACS Nano **12**, 3477 (2018).

[34] X.-G. Zhao, G. M. Dalpian, Z. Wang, and A. Zunger, Polymorphous nature of cubic halide perovskites, Phys. Rev. B **101**, 155137 (2020).

[35] X.-G. Zhao, Z. Wang, O. I. Malyi, and A. Zunger, Effect of static local distortions vs. dynamic motions on the stability and band gaps of cubic oxide and halide perovskites, Mater. Today **49**, 107 (2021).

[36] K. Miyata, D. Meggiolaro, M. T. Trinh, P. P. Joshi, E. Mosconi, S. C. Jones, F. De Angelis, and X.-Y. Zhu, Large polarons in lead halide perovskites, Sci. Adv. **3**, e1701217 (2017).

[37] B. Guzelturk, T. Winkler, T. W. Van de Goor, M. D. Smith, S. A. Bourelle, S. Feldmann, M. Trigo, S. W. Teitelbaum, H.-G. Steinrück, and A. Gilberto, *et al.*, Visualization of dynamic polaronic strain fields in hybrid lead halide perovskites, Nat. Mater. **20**, 618 (2021).

[38] X.-G. Zhao, D. Yang, Y. Sun, T. Li, L. Zhang, L. Yu, and A. Zunger, Cu–In halide perovskite solar absorbers, J. Am. Chem. Soc. **139**, 6718 (2017).

[39] V.-A. Ha, G. Volonakis, H. Lee, M. Zacharias, and F. Giustino, Quasiparticle band structure and phonon-induced band gap renormalization of the lead-free halide double perovskite $Cs_2InAgCl_6$, J. Phys. Chem. C **125**, 21689 (2021).

[40] M. Zacharias, G. Volonakis, F. Giustino, and J. Even, Anharmonic electron-phonon coupling in ultrasoft and locally disordered perovskites, npj Comput. Mater. **9**, 153 (2023).

[41] M. Jocić and N. Vukmirović, Ab-initio calculations of temperature dependent electronic structures of inorganic halide perovskite materials, Phys. Chem. Chem. Phys. **25**, 29017 (2023).

[42] N. Yazdani, *et al.*, Coupling to octahedral tilts in halide perovskite nanocrystals induces phonon-mediated attractive interactions between excitons, Nat. Phys. **20**, 47 (2024).

[43] J. A. Steele, P. Puech, M. Keshavarz, R. Yang, S. Banerjee, E. Debroye, C. W. Kim, H. Yuan, N. H. Heo, and J. Vanacken, *et al.*, Giant electron–phonon coupling and deep conduction band resonance in metal halide double perovskite, ACS Nano **12**, 8081 (2018).

[44] J. Leveillee, G. Volonakis, and F. Giustino, Phonon-limited mobility and electron–phonon coupling in lead-free halide double perovskites, J. Phys. Chem. Lett. **12**, 4474 (2021).

[45] R. Kentsch, M. Scholz, J. Horn, D. Schlettwein, K. Oum, and T. Lenzer, Exciton dynamics and electron–phonon coupling affect the photovoltaic performance of the $Cs_2AgBiBr_6$ double perovskite, J. Phys. Chem. C **122**, 25940 (2018).

[46] Y. Yin, W. Tian, J. Leng, J. Bian, and S. Jin, Carrier transport limited by trap state in $Cs_2AgBiBr_6$ double perovskites, J. Phys. Chem. Lett. **11**, 6956 (2020).

[47] B. Wu, W. Ning, Q. Xu, M. Manjappa, M. Feng, S. Ye, J. Fu, S. Lie, T. Yin, and F. Wang, *et al.*, Strong self-trapping by deformation potential limits photovoltaic performance in bismuth double perovskite, Sci. Adv. **7**, eabd3160 (2021).

[48] J. Gebhardt and C. Elsässer, The electronic structure of $Cs_2AgBiBr_6$ at room temperature, Phys. Status Solidi **259**, 2200124 (2022).

[49] J. Gebhardt, W. Wei, and C. Elsässer, Efficient modeling workflow for accurate electronic structures of hybrid perovskites, J. Phys. Chem. C **125**, 18597 (2021).

[50] A. D. Wright, L. R. Buizza, K. J. Savill, G. Longo, H. J. Snaith, M. B. Johnston, and L. M. Herz, Ultrafast excited-state localization in $Cs_2AgBiBr_6$ double perovskite, J. Phys. Chem. Lett. **12**, 3352 (2021).

[51] N. K. Tailor, S. K. Saini, P. Yadav, M. Kumar, and S. Satapathi, Elucidating polaron dynamics in $Cs_2AgBiBr_6$ double perovskite, J. Phys. Chem. Lett. **14**, 730 (2023).

[52] N. K. Tailor, N. Parikh, P. Yadav, and S. Satapathi, Dielectric relaxation and polaron hopping in $Cs_2AgBiBr_6$ halide double perovskites, J. Phys. Chem. C **126**, 10199 (2022).

[53] J. Zheng, C. Lin, C. Lin, R. Guo, and B. Huang, Strong anharmonic phonon renormalization and dominant role of wave-like tunnelling of phonons in thermal transport in lead-free halide double perovskites, Preprint ArXiv:2301.12273 (2023).

[54] K. Miyata, T. L. Atallah, and X.-Y. Zhu, Lead halide perovskites: Crystal-liquid duality, phonon glass electron crystals, and large polaron formation, Sci. Adv. **3**, e1701469 (2017).

[55] C. Katan, A. D. Mohite, and J. Even, Entropy in halide perovskites, Nat. Mater. **17**, 377 (2018).

[56] F. Bertolotti, L. Protesescu, M. V. Kovalenko, S. Yakunin, A. Cervellino, S. J. Billinge, M. W. Terban, J. S. Pedersen, N. Masciocchi, and A. Guagliardi, Coherent nanotwins and dynamic disorder in cesium lead halide perovskite nanocrystals, ACS Nano **11**, 3819 (2017).

[57] M. Sakata, J. Harada, M. Cooper, and K. Rouse, A neutron diffraction study of anharmonic thermal vibrations in cubic $CsPbX_3$, Acta Crystallogr. Section A: Crystal Phys. Diffr. Theor. General Crystallogr. **36**, 7 (1980).

[58] M. Simoncelli, N. Marzari, and F. Mauri, Unified theory of thermal transport in crystals and glasses, Nat. Phys. **15**, 809 (2019).

[59] T. Haeger, R. Heiderhoff, and T. Riedl, Thermal properties of metal-halide perovskites, J. Mater. Chem. C **8**, 14289 (2020).

[60] E. Haque and M. A. Hossain, Origin of ultra-low lattice thermal conductivity in Cs_2BiAgX_6 ($X = $ Cl, Br) and its impact on thermoelectric performance, J. Alloys Compd. **748**, 63 (2018).

[61] J. Klarbring, O. Hellman, I. A. Abrikosov, and S. I. Simak, Anharmonicity and ultralow thermal conductivity in lead-free halide double perovskites, Phys. Rev. Lett. **125**, 045701 (2020).

[62] A. Cohen, T. M. Brenner, J. Klarbring, R. Sharma, D. H. Fabini, R. Korobko, P. K. Nayak, O. Hellman, and O. Yaffe, Diverging expressions of anharmonicity in halide perovskites, Adv. Mater. **34**, 2107932 (2022).

[63] L. Schade, S. Mahesh, G. Volonakis, M. Zacharias, B. Wenger, F. Schmidt, S. V. Kesava, D. Prabhakaran, M. Abdi-Jalebi, M. Lenz, F. Giustino, G. Longo, P. G. Radaelli, and H. J. Snaith, Crystallographic, optical, and electronic properties of the $Cs_2AgBi_{1-x}In_xBr_6$ double perovskite: Understanding the fundamental photovoltaic efficiency challenges, ACS Energy Lett. **6**, 1073 (2021).

[64] S. P. Girdzis, Y. Lin, L. Leppert, A. H. Slavney, S. Park, K. W. Chapman, H. I. Karunadasa, and W. L. Mao, Revealing local disorder in a silver-bismuth halide perovskite upon compression, J. Phys. Chem. Lett. **12**, 532 (2020).

[65] F. Ye, Y. Liu, R. Whitfield, R. Osborn, and S. Rosenkranz, Implementation of cross correlation for energy discrimination on the time-of-flight spectrometer CORELLI, J. Appl. Crystallogr. **51**, 315 (2018).

[66] See Supplemental Materials at http://link.aps.org/supplemental/10.1103/PRXEnergy.3.013014 for details of neutron and x-ray diffuse scattering; inelastic neutron scattering data fitting; harmonic phonon calculations; *ab initio* molecular dynamics, anharmonic phonon renormalization, and machine-learning molecular dynamics; discussion of low-temperature soft mode and ground states. Supplemental Material also contains Refs. [24,30,61,64,67–69,73–78, 80–90].

[67] O. Hellman, I. Abrikosov, and S. Simak, Lattice dynamics of anharmonic solids from first principles, Phys. Rev. B **84**, 180301 (2011).

[68] O. Hellman, P. Steneteg, I. A. Abrikosov, and S. I. Simak, Temperature dependent effective potential method for accurate free energy calculations of solids, Phys. Rev. B **87**, 104111 (2013).

[69] O. Hellman and I. A. Abrikosov, Temperature-dependent effective third-order interatomic force constants from first principles, Phys. Rev. B **88**, 144301 (2013).

[70] A. Ferreira, S. Paofai, A. Létoublon, J. Ollivier, S. Raymond, B. Hehlen, B. Rufflé, S. Cordier, C. Katan, and J. Even, *et al.*, Direct evidence of weakly dispersed and strongly anharmonic optical phonons in hybrid perovskites, Commun. Phys. **3**, 1 (2020).

[71] We note that during the cubic-tetragonal phase transition, the unit cell does not change except for the elongated ratio $c/a > 1$. As a result, the BZ is nearly the same in tetragonal and cubic phases but with the reciprocal c^* parameter shortened. Thus, we keep the same notation for high-symmetry BZ points and K points refer to (0.75, 0.75, 0) in planes $L = $ integer.

[72] M. J. Krogstad, S. Rosenkranz, J. M. Wozniak, G. Jennings, J. P. C. Ruff, J. T. Vaughey, and R. Osborn, Reciprocal space imaging of ionic correlations in intercalation compounds, Nat. Mater. **19**, 63 (2020).

[73] G. Kresse and J. Hafner, Ab initio molecular dynamics for liquid metals, Phys. Rev. B **47**, 558 (1993).

[74] G. Kresse and J. Hafner, Ab initio molecular-dynamics simulation of the liquid-metal–amorphous-semiconductor transition in germanium, Phys. Rev. B **49**, 14251 (1994).

[75] G. Kresse and J. Furthmüller, Efficiency of ab-initio total energy calculations for metals and semiconductors using a plane-wave basis set, Comput. Mater. Sci. **6**, 15 (1996).

[76] G. Kresse and J. Furthmüller, Efficient iterative schemes for ab initio total-energy calculations using a plane-wave basis set, Phys. Rev. B **54**, 11169 (1996).

[77] A. Togo and I. Tanaka, First principles phonon calculations in materials science, Scr. Mater. **108**, 1 (2015).

[78] F. Ji, J. Klarbring, F. Wang, W. Ning, L. Wang, C. Yin, J. S. M. Figueroa, C. K. Christensen, M. Etter, and T. Ederth, *et al.*, Lead-free halide double perovskite $Cs_2AgBiBr_6$ with decreased band gap, Angew. Chem. **132**, 15303 (2020).

[79] G. L. Squires, *Introduction to the Theory of Thermal Neutron Scattering* (Dover Publications, Mineola N.Y., 1996).

[80] J. Sun, R. C. Remsing, Y. Zhang, Z. Sun, A. Ruzsinszky, H. Peng, Z. Yang, A. Paul, U. Waghmare, and X. Wu, *et al.*, Accurate first-principles structures and energies of diversely bonded systems from an efficient density functional, Nat. Chem. **8**, 831 (2016).

[81] H. J. Monkhorst and J. D. Pack, Special points for Brillouin-zone integrations, Phys. Rev. B **13**, 5188 (1976).

[82] H. Wang, L. Zhang, J. Han, and E. Weinan, Deepmd-kit: A deep learning package for many-body potential energy representation and molecular dynamics, Comput. Phys. Commun. **228**, 178 (2018).

[83] S. Plimpton, Fast parallel algorithms for short-range molecular dynamics, J. Comput. Phys. **117**, 1 (1995).

[84] A. Zhedludhev, Reslib, https://neutron.ethz.ch/Methods/reslib.html.

[85] M. Popovici, On the resolution of slow-neutron spectrometers. IV. the triple-axis spectrometer resolution function, spatial effects included, Acta Crystallogr. Section A: Crystal Phys. Diffr. Theor. General Crystallogr. **31**, 507 (1975).

[86] J. P. Perdew, K. Burke, and M. Ernzerhof, Generalized gradient approximation made simple, Phys. Rev. Lett. **77**, 3865 (1996).

[87] G. I. Csonka, J. P. Perdew, A. Ruzsinszky, P. H. Philipsen, S. Lebègue, J. Paier, O. A. Vydrov, and J. G. Ángyán, Assessing the performance of recent density functionals for bulk solids, Phys. Rev. B **79**, 155107 (2009).

[88] Debyer, https://debyer.readthedocs.io/en/latest/.

[89] H. T. Stokes and D. M. Hatch, Findsym: Program for identifying the space-group symmetry of a crystal, J. Appl. Crystallogr. **38**, 237 (2005).

[90] D. M. H. H. T. Stokes and B. J. Campbell, Findsym, isotropy software suite, iso.byu.edu.